PERGAMON

International Journal of Heat and Mass Transfer 41 (1998) 3431–3440

International Journal of
HEAT and MASS
TRANSFER

# Convective and radiative internal heat transfer augmentation with fiber arrays

A. R. Martin[a], C. Saltiel[b,*], J. Chai[c], W. Shyy[d]

[a] *Department of Mechanical Engineering, University of Florida, Gainesville, FL 32611, U.S.A.*
[b] *Synergetic Technologies, Inc., Delmar, NY 12054, U.S.A.*
[c] *Department of Mechanical Engineering, Tennessee Technological University, Cookeville, TN 38505, U.S.A.*
[d] *Department of Aerospace Engineering, Mechanics and Engineering Science, University of Florida, Gainesville, FL 32611, U.S.A.*

Received 10 July 1997; in final form 29 January 1998

**Abstract**

A detailed numerical study is performed to investigate radiative and convective heat transfer enhancement in pipes filled with small diameter ($\sim 100$ $\mu$m) silicon carbide fibers. Radiation between fibers and the tube wall, conduction within fibers and convection from the fibers to the surrounding fluid drive the heat transfer enhancement. Macroscopic (porous media) modeling is used to determine the velocity, pressure, and temperatures fields for periodic fiber arrays of various porosites under laminar flow conditions ($Re_D = 1000$). Key features of the macroscopic model include two-dimensional effects, nongray radiative exchange, and the relaxation of the local thermodynamic equilibrium assumption. Results show that fiber arrays increase heat transfer largely by the radiative mode, with significant enhancement shown for porosities as high as 0.99. The increased pressure drop due to the presence of the fibers rises monotonically as the porosity is reduced. © 1998 Elsevier Science Ltd. All rights reserved.

**Nomenclature**

| | |
|---|---|
| $a$ | specific surface area |
| $c_p$ | specific heat |
| $C$ | permeability parameter |
| $d$ | fiber diameter |
| $D$ | tube diameter |
| $h$ | convective heat transfer coefficient |
| $I_\lambda$, $i_{b\lambda}$ | spectral and blackbody radiative intensities |
| $K$, $\boldsymbol{K}$ | permeability scalar and tensor |
| $k$, $\boldsymbol{k}$ | thermal conductivity scalar and tensor; complex index of refraction |
| $L$ | tube length |
| $n$ | real index of refraction |
| $Nu_d$ | Nusselt number |
| $p$ | pressure |
| $q$, $\boldsymbol{q}_R$ | heat flux scalar and radiative heat flux vector |
| $Q_a$ | absorption efficiency factor |
| $r$ | radial coordinate |
| $Re_D$ | tube Reynolds number |
| $\boldsymbol{S}_f$ | interfacial momentum source tensor |
| $T$ | temperature |
| $u$ | axial velocity |
| $\boldsymbol{u}$ | velocity vector |
| $U$ | average velocity |
| $V$ | representative elementary volume (REV) |
| $z$ | axial coordinate. |

*Greek symbols*

| | |
|---|---|
| $\beta_\lambda$ | spectral extinction coefficient |
| $\gamma$ | circumferential coordinate |
| $\Gamma$ | scalar or vector quantity |
| $\varepsilon$ | volume fraction |
| $\bar{\varepsilon}_w$ | wall emissivity |
| $\theta$ | polar angle |
| $\Theta$ | heat exchanger effectiveness |
| $\kappa_\lambda$, $\bar{\kappa}$ | spectral and Planck-mean absorption coefficients |
| $\lambda$ | wavelength |
| $\mu$ | dynamic viscosity |
| $\rho$ | density |
| $\sigma_\lambda$ | spectral scattering coefficient |
| $\tau_D$ | optical depth |
| $\phi$ | azimuthal angle |

---

* Corresponding author.

0017–9310/98 $19.00 © 1998 Elsevier Science Ltd. All rights reserved
PII: S0017-9310(98)00066-0

| | |
|---|---|
| $\Phi_\lambda$ | scattering phase function |
| $\Psi$ | scattering angle |
| $\omega$ | wave number |
| $\Omega$ | solid angle. |

*Subscripts and superscripts*

| | |
|---|---|
| b | bulk |
| c | centerline |
| e | effective |
| $f$ | fluid phase |
| $fs$ | fluid–solid interface |
| h | homogeneous |
| i | inlet |
| $k$ | phase |
| $s$ | solid phase |
| w | wall |
| * | nondimensional quantity. |

## 1. Introduction

Economic and environmental incentives continue to reward innovative concepts for improving heat exchanger performance and durability. This is especially true for equipment operating under highly corrosive, high temperature conditions, such as in coal-fired boilers or waste-to-energy incinerators where corrosion is greatly exacerbated by excessive operating temperatures [1–3]. At these high temperatures ($>600^\circ$C), radiative transport can play a significant role in promoting heat transfer provided the necessary transfer mechanisms are present. For example, the addition of solid particles in a flow field can increase heat transfer coefficients by as much as a factor of 20 [4]. A major drawback, of course, is the damage these particles can have on system components. A stationary porous insert which acts as a participating media avoids this problem but, unless the porosity is very high, the insert can introduce significant pressure losses.

Im and Ahluwalia [5] recently investigated an insert consisting of long, small diameter ($\sim 100\ \mu$m) fiber arrays aligned in the flow direction. If the fiber arrays are highly porous, pressure losses will be reduced. However, if they are too porous, contribution to promoting radiative heat transfer will be inconsequential. As an introductory study, the Im and Ahluwalia investigation [5] did an excellent job in providing quantitative evidence of heat transfer enhancement and pressure losses in fiber filled tubes. Based on their very positive results, we believe a more in-depth investigation is merited; one which analyzes fiber/fluid interaction more closely. In particular, because the interest is in highly porous arrays and only the fibers are active in radiation transfer (the fluid does not participate), local thermodynamic equilibrium between the fluid and fibers must be examined; such effects have shown to be important in nuclear systems [6, 7].

In this study we model the flow as porous media, and couple conduction, convection, and radiation within the global domain. Silicon carbide (SiC) is selected as the fiber material, as it was identified by Im and Ahluwalia [5] as having the best radiative characteristics out of a number of ceramic and metallic compounds. The analysis of Im and Ahluwalia [5] is extended by detailed numerical simulations which account for multidimensional effects and the macroscopic coupling of the heat transfer modes. In addition, emphasis is placed on pipe wall temperature reduction as a performance criteria. The sensitivity of porosity is closely studied for laminar flow conditions.

## 2. Analysis

In the analysis of flow through porous media, it is common to simplify the complex nature of flow around the solid structure by volume averaging of the microscopic flow equations [8]. The volume average of any scalar or vector quantity $\Gamma_k$, associated with phase $k$, is defined as

$$\langle \Gamma_k \rangle = \frac{1}{V}\int_V \Gamma_k \, \mathrm{d}V \tag{1}$$

where $V$ is the representative elementary volume (REV). ($\Gamma_k$ is zero in regions not occupied by phase $k$.) The intrinsic volume average is defined as

$$\langle \Gamma_k \rangle^k = \frac{1}{V_k}\int_{V_k} \Gamma_k \, \mathrm{d}V \tag{2}$$

and may be related to the total volume average by $\varepsilon_k \langle \Gamma_k \rangle^k = \langle \Gamma_k \rangle$, where $\varepsilon_k$ is the volume fraction of phase $k$. For flows in fiber arrays, two distinct phases are present: fluid phase $f$ and solid phase $s$. For steady state, incompressible flow with spatially uniform properties and volume fraction, the volume averaged equations of continuity, momentum, and energy for the fluid phase are as follows [6, 8, 9]:

$$\nabla \cdot \langle \mathbf{u}_f \rangle = 0 \tag{3}$$

$$\frac{\rho_f}{\varepsilon_f^2}\langle \mathbf{u}_f \rangle \cdot \nabla \langle \mathbf{u}_f \rangle = -\nabla \langle p_f \rangle^f + \frac{\mu_f}{\varepsilon_f}\nabla^2 \langle \mathbf{u}_f \rangle - \boldsymbol{S}_f \tag{4}$$

$$\rho_f c_{p,f} \nabla \cdot \langle T_f \rangle^f \langle \mathbf{u}_f \rangle = \boldsymbol{k}_{\mathrm{e}f} \varepsilon_f \nabla^2 \langle T_f \rangle^f + h_{fs} a_{fs} (\langle T_s \rangle^s - \langle T_f \rangle^f). \tag{5}$$

In the above expressions, $\boldsymbol{S}_f$ is the interfacial momentum source term tensor, $\boldsymbol{k}_{\mathrm{e}f}$ the effective fluid thermal conductivity tensor, $h_{fs}$ is the interfacial convection coefficient, and $a_{fs}$ the specific surface area of the interface; the other variables are listed in the nomenclature. Since the solid phase is stationary, only the energy equation needs to be considered:

$$0 = \boldsymbol{k}_{\mathrm{e}s} \varepsilon_s \nabla^2 \langle T_s \rangle^s - h_{fs} a_{fs} (\langle T_s \rangle^s - \langle T_f \rangle^f) - \langle \nabla \cdot \mathbf{q}_{\mathrm{R}} \rangle \tag{6}$$

where $\langle \nabla \cdot \mathbf{q}_{\mathrm{R}} \rangle$ is the divergence of the radiative heat flux, which is not included in the fluid phase since the fluid is transparent. Treatment of the source terms resulting from the volume averaging procedure is presented below.

### 2.1. Momentum and energy source terms

Darcy flow is considered for the functional form of the interfacial momentum source term tensor $\boldsymbol{S}_f$:

$$\boldsymbol{S}_f = \frac{\mu_f \langle u_f \rangle}{\boldsymbol{K}} \tag{7}$$

where $\boldsymbol{K}$ is the Darcian permeability tensor. Non-Darcy effects should not be important in this situation since the radial velocity components are small and flow longitudinal to the fiber array does not exhibit any inertial effects due to vortex generation or wakes. Åström et al. [10] have reviewed a number of investigations of Darcian flow through aligned fiber beds; they report the functional form of $\boldsymbol{K}$ as

$$\frac{K_z}{C_z} = \frac{K_r}{C_r} = \frac{d^2}{16\varepsilon_s} \tag{8}$$

where $K_z$ and $K_r$ are the permeabilities in the axial and radial directions for a square array, and $d$ is the fiber diameter. Parameters $C_z$ and $C_r$ have been obtained by Drummond and Tahir [11] from Stokes flow analyses:

$$C_z = \ln\left(\frac{1}{\varepsilon_s}\right) - 1.476 + 2\varepsilon_s - 0.5\varepsilon_s^2 - \frac{0.05097\varepsilon_s^4}{1 + 1.52\varepsilon_s^2} \tag{9}$$

and

$$C_r = \frac{1}{2}\left(\ln\left(\frac{1}{\varepsilon_s}\right) - 1.476 + \frac{2\varepsilon_s - 0.796\varepsilon_s^2}{10.489\varepsilon_s - 1.60\varepsilon_s^2}\right). \tag{10}$$

Figure 1 shows the functional relationship of the permeability, nondimensionalized by the square of the fiber diameter $d$, with respect to the fluid volume fraction. In qualitative terms, the square root of the permeability is indicative of the characteristic pore length scale [8]. For the range of porosities considered in this study ($0.90 \leqslant \varepsilon_f \leqslant 0.99$), the size of the pores is at least two orders of magnitude smaller than the pipe diameter.

Since the fluid volume fraction is large, the effective conductivity of the fluid phase is taken as the actual fluid conductivity, or

$$k_{f,r} = k_{f,z} = k_f. \tag{11}$$

Similar to the fluid phase, the axial conductivity for the solid is

$$k_{s,z} = k_s \tag{12}$$

while $k_{s,r} = 0$ because the fibers are not connected radially. The determination of the interfacial heat transfer coefficient $h_{fs}$ is found via the equivalent annulus formulation presented by Sparrow et al. [12], which is an accurate approximation for longitudinal flows in fiber arrays with high porosity. The Nusselt number $Nu_d = h_{fs}d/k_f$ is shown in Fig. 1 as a function of the fluid volume fraction. Finally, the interfacial surface area $a_{fs} = 4\varepsilon_s/d$ for square arrays.

### 2.2. Radiative transport

Radiation heat transfer has been investigated in a number of porous media applications, as reviewed by Kaviany and Singh [13] and Tien and Vafai [14]. The divergence of the radiative heat flux is

$$\langle \nabla \cdot \mathbf{q}_\mathrm{R} \rangle = \int_0^\infty \kappa_\lambda \left(4\pi I_{\mathrm{b}\lambda} - \int_{4\pi} I_\lambda \,\mathrm{d}\Omega\right) \mathrm{d}\lambda \tag{13}$$

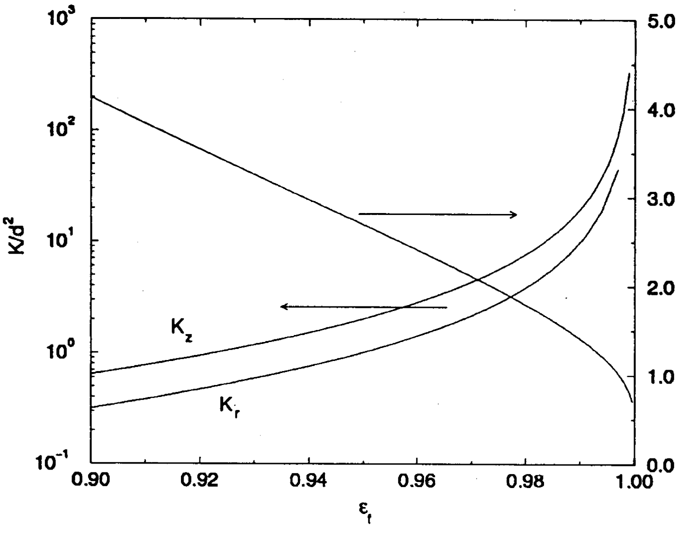

Fig. 1. Permeability and Nusselt number vs. fluid volume fraction, $d = 150\ \mu$m.

where $\kappa_\lambda$ is the absorption coefficient, $I_{b\lambda}$ the blackbody intensity, $I_\lambda$ the radiative intensity, and $\lambda$ the wavelength. The radiative intensity is found via the radiative transfer equation (RTE):

$$\mathbf{s}\cdot\nabla I_\lambda = \kappa_\lambda I_{\mathrm{b}\lambda} - \beta_\lambda I_\lambda + \frac{\sigma_\lambda}{4\pi}\int_{4\pi} I_\lambda \Phi_\lambda \,\mathrm{d}\Omega \tag{14}$$

where $\beta_\lambda$ is the extinction coefficient, $\sigma_\lambda$ the scattering coefficient, and $\Phi_\lambda$ the scattering phase function. Because the fluid is nonparticipating, $I_{\mathrm{b}\lambda}$ is computed based upon the local solid temperature $\langle T_s\rangle^s$, and the radiative source term is not included in the fluid phase energy equation.

In order to determine the absorption and scattering coefficients, the real and complex indices of refraction, $n$ and $k$, must be known for the given fiber material. Palik [15] present the optical properties for a number of solid materials, including SiC. An oscillator model is reported to be in good agreement with experimental results in the 2–22 $\mu$m range:

$$(n-ik)^2 = \varepsilon_\infty\left(1+\frac{\omega_L^2-\omega_T^2}{\omega_T^2-\omega^2+i\omega_\Gamma\omega}\right) \tag{15}$$

where $\omega$ is the wavenumber, $\omega_L = 969$ cm$^{-1}$, $\omega_T = 793$ cm$^{-1}$, $\omega_\Gamma = 4.76$ cm$^{-1}$, and $\varepsilon_\infty = 6.7$ (considering the ordinary ray). Figure 2 illustrates $n$ and $k$ as a function of wavelength for SiC. It can be seen that the optical properties are a strong function of wavelength, with an abrupt change in $n$ and $k$ shown around 10 $\mu$m. Next, the absorption efficiency factor $Q_a$ is found from solution of the electromagnetic wave equation. Following Bohren and Huffman [16], the wavelength dependence of $Q_a$ is computed as a function of the size parameter $x = \pi d/\lambda$ and optical properties $n$ and $k$ (see inset of Fig. 3). The absorption coefficient $\kappa_\lambda$ is related to the absorption efficiency factor by

$$\kappa_\lambda = Q_a\left(\frac{4\varepsilon_s}{d}\right). \tag{16}$$

The stepwise gray approximation [17] is used to simplify the nongray treatment, and $Q_a$ is subdivided into five nongray zones as shown in Fig. 3. Zones I, III, and V have constant $\kappa_\lambda$ values, with $\kappa_{\mathrm{I}} = 0$ (i.e. transparent) in Zone I, and $\kappa_{\mathrm{v}}$ in Zone V extrapolated from Zone IV. Zones II and IV exhibit gas-like absorptive behavior, hence a special procedure is employed to determine $\kappa$ for each of these zones. As described by Modest [17], $\kappa$ and the bandwidth $\Delta\lambda$ are chosen so that the stepwise gray approximation predicts the correct band absorptance for both optically thin and optically thick situations. Thus, $\kappa$ and $\Delta\lambda$ for these zones are found via the following relations: optically thin limit,

$$\int \kappa_\lambda \,\mathrm{d}\lambda = \kappa\Delta\lambda \tag{17}$$

and optically thick limit,

$$\int(1-e^{-\kappa_\lambda X_m})\,\mathrm{d}\lambda = \Delta\lambda(1-e^{-\kappa X_m}) \tag{18}$$

where $X_m$ is the mean beam length of the media, taken as 0.94 $D$ for an infinite circular cylinder [17]. Figure 3 shows $\kappa$ for each of the four radiatively participating zones as a function of porosity.

Figure 4 shows the scattering phase function $\Phi$ for a given scattering angle $\Psi$, as calculated by the diffraction theory approximation [16]:

$$\Phi(\Psi) = \frac{\pi}{4x}\left[\left(\frac{1+\cos\Psi}{\pi}\right)\left(\frac{\sin(x\sin\Psi)}{\sin\Psi}\right)\right]^2. \tag{19}$$

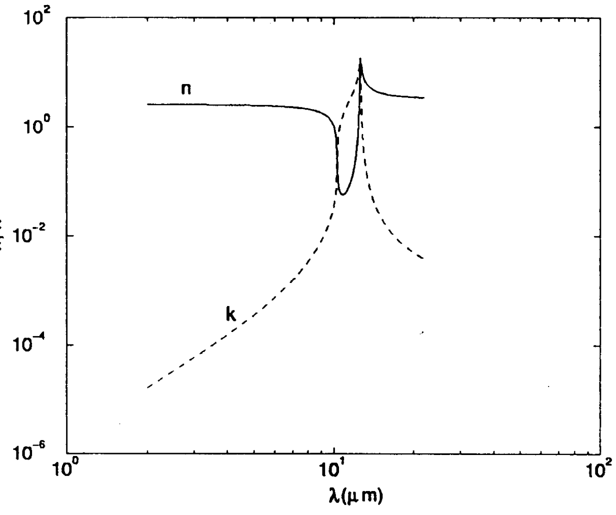

Fig. 2. Optical properties of SiC vs. wavelength.

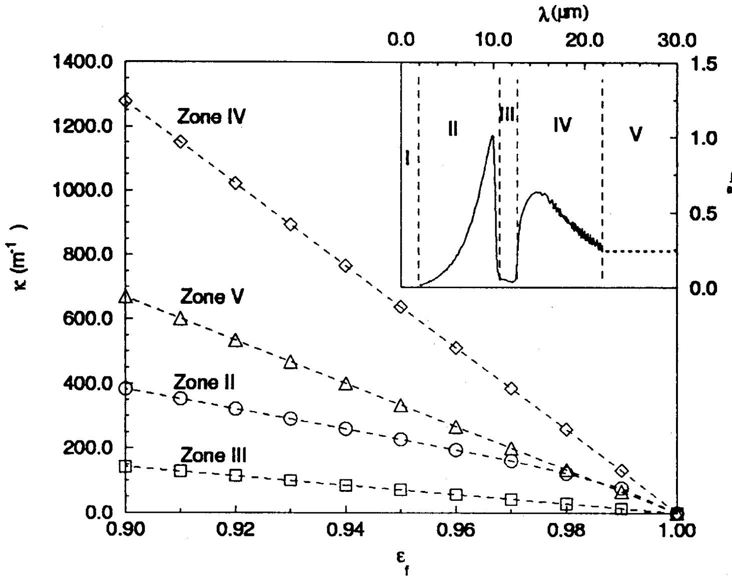

Fig. 3. Absorption coefficient vs. fluid volume fraction for SiC fibers, $d = 150$ $\mu$m (inset: absorption efficiency factor vs. wavelength).

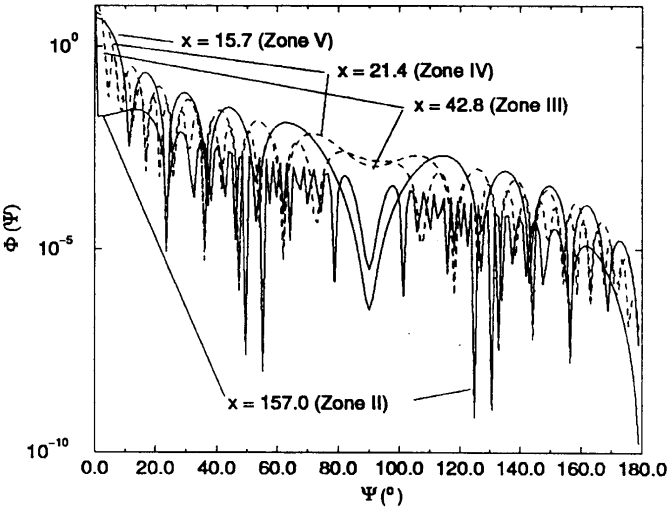

Fig. 4. Scattering phase function vs. scattering angle for SiC fibers, $d = 150$ $\mu$m.

For the size parameters shown in the figure, which cover the range of values of interest for this application, Φ is shown to be highly forward scattering. Since the phase function varies over several orders of magnitude over only a few degrees of scattering angle, the scattering component of radiation is treated as transmission [17].

### 2.3. Numerical approach

A finite volume-based numerical procedure based on the SIMPLE algorithm [18] is used to solve the macroscopic equations (3)–(5) in two-dimensional axisymmetric coordinates $r$ and $z$, with the hybrid scheme [18] used for convective terms. The solution procedure to the RTE is described in Moder et al. [19], with slight modification made to the treatment of the spatial grid in the circumferential direction, $\gamma$. Instead of considering a fixed number of control volumes for $0 < \gamma < 2\pi$, only a single control volume is considered in this direction in order to minimize computational effort. Rotational symmetry is then used to assign the boundary intensity values on the circumferential interfaces, and care is taken to ensure that the circumferential control volume $\Delta\gamma$ is consistent with the azimuthal control volume $\Delta\phi$. The spatial grid is further divided into $10 \times 40$ control volumes in the radial and axial directions, respectively. Also, the angular grid is divided into $8 \times 16$ control volumes in the $\theta$ and $\phi$ directions.

To check the validity of the model, the numerical study presented by Einstein [20] was selected as one benchmark. This study considers a radiatively participating gray gas flowing through a pipe with black walls and constant temperature (750 K); the inlet and outlet of the pipe are black, with $T_i = 300$ K. Figure 5 shows a comparison to the Einstein study, which features the nondimensional outlet temperature vs. optical depth for a number of conduction-to-radiation ratios. Our results show a variation of no more than 5% from values reported by Einstein. In addition, the accuracy of the radiation calculations was checked against results presented in Chui et al. [21], who determined an exact solution to radiative transfer in a cylindrical enclosure with cold, black walls and uniform (gray) medium temperature. The nondimensionalized wall heat flux is shown in Fig. 6 as a function of axial location. Good agreement (less than 5% deviation) can be seen for three optical depths shown, with the current results approaching the exact solution as the azimuthal angular discretization is further refined. (It should be noted that the spatial grid is $16 \times 30$ for this comparison.)

For the present application, no-slip and no-penetration boundary conditions are imposed at the tube wall, with the outlet velocity extrapolated in the streamwise direction. The inlet and outlet of the tube are black, and a constant heat flux $q_w = 1800$ W m$^{-2}$ is applied to the tube wall, which has a total hemispherical emissivity indicative of unpolished metals ($\bar{\varepsilon}_w = 0.3$ [17]). The inlet fluid temperature is fixed at 300 K, and the outlet fluid temperature, along with the inlet and outlet solid temperatures, are extrapolated from the interior. Fluid and solid are considered to be isothermal at the tube wall, and the wall temperature is found via a balance of the wall heat flux, conduction and radiation. A tube Reynolds number, $Re_D$, of 1000 is considered, with a fully developed laminar (parabolic) profile assigned at the inlet. The physical properties of the fluid (air) and SiC are taken at 300 K, and can be found in Incropera and DeWitt [22]; see Table 1 for their values, along with other input parameters.

## 3. Results

One consequence of employing fiber arrays is the alteration of the velocity profile due to the strong flow resistance offered by the porous media. Figure 7 illustrates the nondimensional centerline velocity $u_c^*$ as a function of axial length for a range of porosity values. The value of $u_c^*$ is defined as

$$u_c^* = \frac{\langle u_f(0,z) \rangle}{U} \tag{20}$$

where $\langle u_f(0,z) \rangle$ is axial centerline velocity and $U$ the average axial velocity. For a porosity of one, the centerline velocity is twice the average velocity, resulting from the fully developed laminar profile. Addition of fiber arrays tends to flatten out the flow within an entry length, which becomes very short as the porosity is reduced.

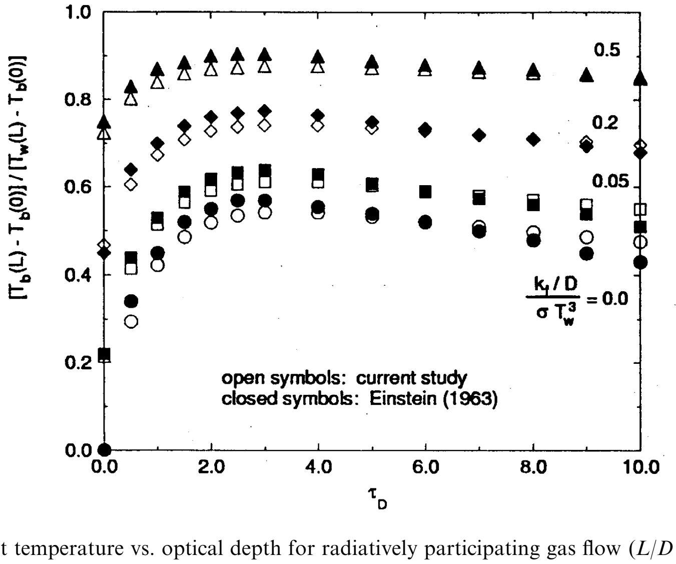

Fig. 5. Nondimensional outlet temperature vs. optical depth for radiatively participating gas flow ($L/D = 5.0$, $Re_D = 1309$, $T_w = 750$ K, and $T_i/T_w = 0.4$).

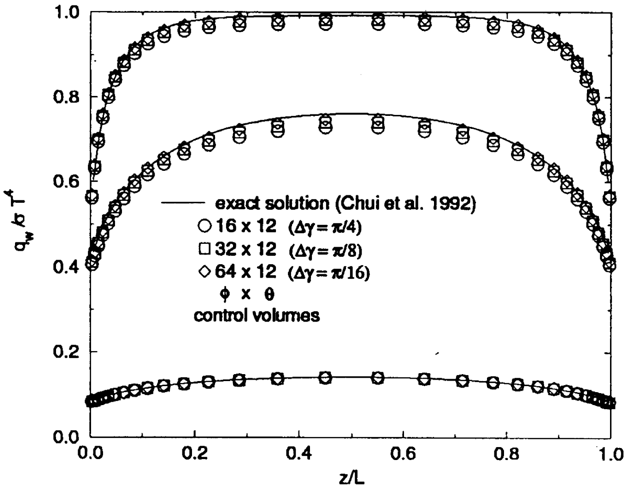

Fig. 6. Nondimensional wall heat flux vs. nondimensional axial length for radiative heat transfer in a cylindrical enclosure with cold walls and uniform medium temperature ($L/D = 1.0$).

Table 1
Input parameters for fiber array analysis

| Parameter | Value |
|---|---|
| $\rho_f$ | 1.23 kg m$^{-3}$ |
| $\mu_f$ | $1.79\times10^{-5}$ N s m$^{-2}$ |
| $c_{p,f}$ | 1006 J kg$^{-1}$ K$^{-1}$ |
| $k_f$ | 0.025 W m$^{-1}$ °C$^{-1}$ |
| $k_s$ | 490 W m−1 °C$^{-1}$ |
| $T_i$ | 300 K |
| $D$ | 0.025 m |
| $L$ | 0.5 m |
| $Re_D$ | 1000 |
| $q_w$ | 1800 W m$^{-2}$ |

In order to quantify the heat transfer enhancement, a heat exchange effectiveness $\Theta(z)$ is defined as

$$\Theta(z) = \frac{T_b(z) - T_b(0)}{T_w(z) - T_b(z)} \tag{21}$$

where $T_b(z)$ and $T_w(z)$ are the bulk and wall temperatures for axial location $z$. The heat exchange effectiveness represents the ratio of the actual heat transfer to the fluid to the maximum possible heat transfer at a given axial location. Figure 8 shows the heat exchange effectiveness at the tube outlet $z = L$ as a function of porosity and optical thickness, where $\tau_D$ is based on the Planck-mean absorption coefficient, $\bar{\kappa}$, evaluated at 580 K. Six different curves of $\Theta(L)$ are shown to illustrate the importance of the heat transfer modes and modeling assumptions, which can be classified as follows: radiative transfer (with conduction and convection) vs. no radiative transfer (i.e. conduction and convection alone); nongray vs. gray radiative transfer; and local thermodynamic equilibrium (LTE) vs. nonequilibrium (denoted non-LTE). The figure shows that the radiative mode of heat transfer is responsible for a significant portion of the heat transfer augmentation. Nongray effects are most important in the optically thin region, while at higher optical depths the difference between gray and nongray radiative transfer is indistinguishable. Also, the results illustrate the importance of nonequilibrium effects, especially at higher optical depths. For the case of nongray radiative transfer with the non-LTE assumption, an optimum in $\Theta(L)$ can be seen at $\tau_D = 5.7$, showing the self-shielding effect which is evident as the fiber array becomes strongly absorbing. With respect to the case of conduction and convection alone, the sharp increase in $\Theta(L)$ as $\varepsilon_f \rightarrow 1.0$ can be attributed to the change in velocity profile from parabolic to flat. The importance of relaxing the LTE assumption for the no radiation case can also be seen, although to a lesser degree.

To assess the pressure drop penalty introduced by the fiber arrays, a nondimensionalized pressure gradient $-\nabla p^*$ is defined as:

$$-\nabla p^* = \frac{-\nabla\langle p_f\rangle^f}{-\nabla p_h} \tag{22}$$

representing the ratio of the pressure gradient with the fiber arrays to the pressure gradient for homogeneous (no fiber) flow. The value of $-\nabla p^*$, also shown in Fig. 8, rises monotonically as the porosity is reduced, attaining values on the order of ten to one thousand times the homogeneous pressure gradient. (At the optimum value of $\Theta(L)$, $-\nabla p^* = 316$.) The comparison to $-\nabla p^*$ as computed by Darcy's law shows that hydraulic entry length effects are not appreciable in this application.

It is also of interest to evaluate heat transport down-

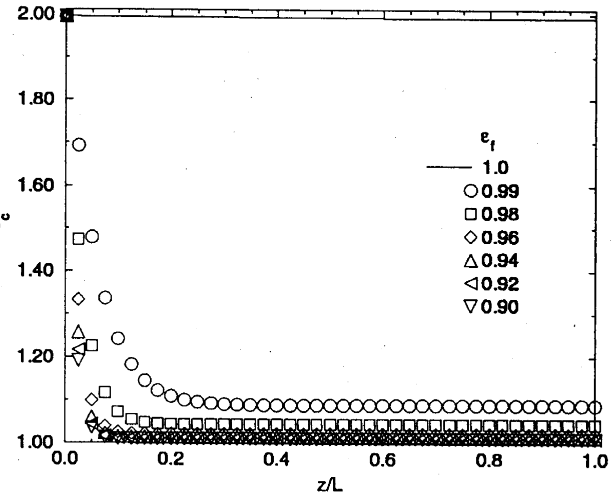

Fig. 7. Nondimensional centerline fluid velocity vs. nondimensional axial length.

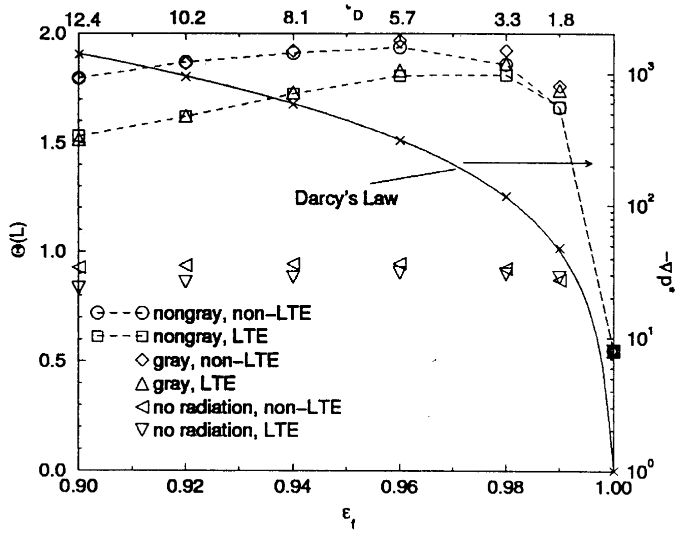

Fig. 8. Heat exchange effectiveness at tube outlet and nondimensinalized pressure drop vs. fluid volume fraction.

stream of the inlet of the tube, as shown in Fig. 9, the heat exchange effectiveness $\Theta(z)$ varies axially for a number of different porosities, with comparison made to the radiation vs. no radiation cases. For the case with radiative transfer included, $\Theta(z)$ initially rises sharply as the porosity is reduced However, the self-shielding effect mentioned above becomes more substantial further downstream as temperatures rise. When radiation is not included, the change in the velocity profile causes a sudden rise in $\Theta(z)$ at the inlet. The dependency of $\Theta(z)$ with porosity can be attributed to the influence of fiber array conductivity at larger solid volume fractions. Leveling off of $\Theta(z)$ at the tube outlet results from the zero gradient boundary condition.

To evaluate the reduction in wall temperature, the nondimensional tube wall temperature, $T_w^*(z) = T_w(z)/T_i$ is shown in Fig. 10 as a function of axial location. At the inlet, little differences can be seen between the radiation and no radiation cases. However, the importance of radiative transfer appears further downstream as this mode of heat transfer becomes more dominant. At the outlet, a significant reduction in wall temperature (about 30% with radiation) is achieved with the fiber arrays even for porosities as high as 0.99. This

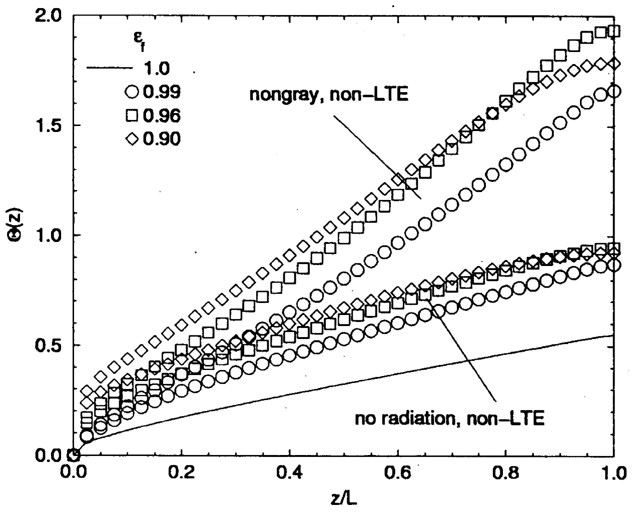

Fig. 9. Heat exchange effectiveness vs. nondimensional axial length.

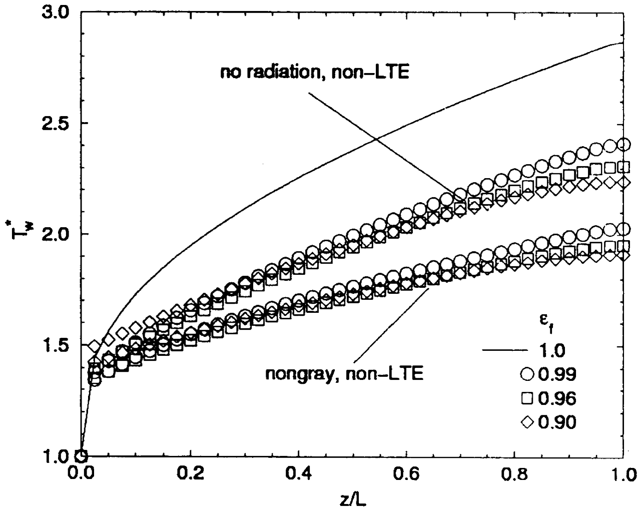

Fig. 10. Nondimensional tube wall temperature vs. nondimensional axial length.

finding shows that high porosity fiber arrays can be employed for applications where only a moderate reduction in wall temperature is required, hence minimizing the pressure drop penalty.

## 4. Concluding remarks

The present study confirms that convective and radiative internal heat transfer augmentation with fiber arrays has great potential as a technique for use in novel heat exchange devices. For the specified parameters,the heat exchange effectiveness was doubled with the fibers arrays as compared to homogeneous flow, resulting in a 30% reduction in tube wall outlet temperature. Although LTE was apparent in the case of conduction and convection alone, significant departure from this assumption could be seen when radiation was included. This finding illustrates the influence of non-LTE effects in cases where radiation is important.

The final merits of the fiber array must, of course, be determined from an overall performance analysis with respect to the given application, especially since the pressure drop penalty is large. Findings from this study point to the need for experimental investigations in order to measure the actual performance of fiber arrays and to validate numerical modeling. Future studies should be conducted to address turbulent flow, since a large number of applications operate in the high Reynolds number range.

## References

[1] Shreir LL. Corrosion. Newnes-Butterworths, Boston, 1976.

[2] Thielsch H, Cone, FM. Corrosion in recovery and refuse-fired boilers. In Proceedings of the 1994 International Joint Power Generation Conference. Kansas City, MO, 1994.

[3] Krause, HH, Vaughan DA, Cover PW, Boyd WK, Oberacker DA. Corrosion and deposits from combustion of solid waste. Journal of Engineering for Power 1977;99:449–59.

[4] Bergles AE. Techniques to augment heat transfer. In : Hartnett JP, Rosenhow WM, Ganic EN, editors. Handbook of Heat Transfer Applications. 2nd ed. New York : McGraw-Hill, 1985.

[5] Im KH, Ahluwalia RK. Radiative enhancement of tube-side heat transfer. International Journal of Heat and Mass Transfer 1994;37(17):2635–46.

[6] Amiri A, Vafai K. Analysis of dispersion effects and non-thermal equilibrium, non-darcian, variable porosity incompressible flow through porous media. International Journal of Heat and Mass Transfer, 1994;37(6):939–54.

[7] Vafai K, Sözen M. Analysis of energy and momentum transport for fluid flow through a porous bed. Journal of Heat Transfer 1990;112:690–9.

[8] Bejan A. Convective Heat Transfer. New York: Wiley-Interscience, 1984.

[9] Cheng P. Heat transfer in geothermal systems. Advances in Heat Transfer 1978;14:1–105.

[10] Åström B, Pipes R, Advani S. On flow through aligned fiber beds and its application to composites processing. Journal of Composite Materials 1992;26(9):1351–73.

[11] Drummond J, Tahir M. Laminar viscous flow through regular arrays of parallel solid cylinders. Journal of Multiphase Flow 1984;10(5):515–40.

[12] Sparrow EM, Loeffler AL and Hubbard HA. Heat transfer to longitudinal laminar flow between cylinders. Journal of Heat Transfer 1961;83:415–22.

[13] Kaviany M, Singh BP. Radiative heat transfer in porous media Advances in Heat Transfer 1993;23:133–86.

[14] Tien CL, Vafai K. Convective and radiative heat transfer in porous media. Advances in Applied Mechanics 1990;27:225–81.

[15] Palik E. Handbook of Optical Constants of Solids II. Orlando : Academic Press, 1985.

[16] Bohren C, Huffman D. Absorption and Scattering of Light by Small Particles. New York : Wiley-Interscience, 1983.

[17] Modest M. Radiative Heat Transfer. New York : McGraw-Hill, 1993.

[18] Patankar SV. Numerical Heat Transfer and Fluid Flow. New York : Hemisphere, 1980.

[19] Moder JP, Chai JC, Parthasarathy G, Lee HS, Patankar SV. Nonaxisymmetric radiative transfer in cylindrical enclosures. Numerical Heat Transfer, Part B 1996;30(4):437–52.

[20] Einstein T. Radiant heat transfer to absorbing gases enclosed in a circular pipe with conduction, gas flow, and internal heat generation. NASA Technical Report TR-156, NASA, 1963.

[21] Chui EH, Raithby GD, Hughes PMJ. Prediction of radiative transfer in cylindrical enclosures with the finite volume method. Journal of Thermophysics and Heat Transfer 1992;6(4):605–11.

[22] Incropera F, DeWitt D. Fundamentals of Heat and Mass Transfer. 2nd ed. New York : John Wiley, 1985.